Supplementary Information for: Valorisation of Bourbon Distillery Waste into Single-source Hybrid Lithium-ion Capacitors

Josiel Barrios Cossio[a], Juan Luis Gómez-Urbano[b], Sandesh Darlami Magar[b], Rodney Andrews[c], Ignacio Martin-Gullon[d,e], Andrea Balducci[b], and Marcelo I. Guzman[*a,f]

[a.] Department of Chemistry, University of Kentucky, Lexington, Kentucky, 40506, United States
[b.] Institute for Technical and Environmental Chemistry, Friedrich Schiller University Jena, and Center for Energy and Environmental Chemistry (CEEC) Jena, Germany
[c.] Center for Applied Energy Research, University of Kentucky, Lexington, Kentucky 40506, United States
[d.] Chemical Engineering Department, University of Alicante, Spain
[e.] Institute of Chemical Process Engineering, University of Alicante, Spain
[f.] Lewis Honors College, University of Kentucky, Lexington, Kentucky 40506, United States.

Corresponding author's email: marcelo.guzman@uky.edu

Section 1. Synthesis and Precursor Material

1.1. HTC

Hydrothermal carbonization (HTC) of bourbon whisky distillery waste (stillage) at 200 °C, under auto-generated pressure (~200 psi), occurs due to its high-water content. Under subcritical conditions, water serves as an eco-friendly reaction medium, transforming stillage into hydrochar.[1] The process is likely initiated by hydrolysis because it has a lower activation energy than other possible reactions.[1, 2] The hydrolysis breaks down hemicellulose into pentoses, cellulose into hexoses, and polysaccharides and lignin into catechols and phenols.[2] Subsequent dehydration of sugars and decarboxylation of organic acids release water and CO_2, reducing H/C and O/C ratios.[3] These transformations generate reactive intermediates that promote aromatization and polymerization, resulting in the formation of a hydrochar. Solid-solid mechanisms, such as torrefaction, may also contribute to the conversion of lignin and polysaccharides.[4] Due to the complex and overlapping nature of these reactions, precisely defining whiskey stillage HTC remains challenging.[5] A proposed pathway for these complex reactions is shown in Scheme 1. The HTC of stillage mainly yields water containing readily degradable aqueous co-products, such as organic and volatile fatty acids, phenols, esters, amino acids, small fractions of lignin and sugars, phosphorus, and nitrogen. It also releases small amounts of gases, such as CO_2, H_2, and CH_4, along with the solid product, hydrochar.[2]

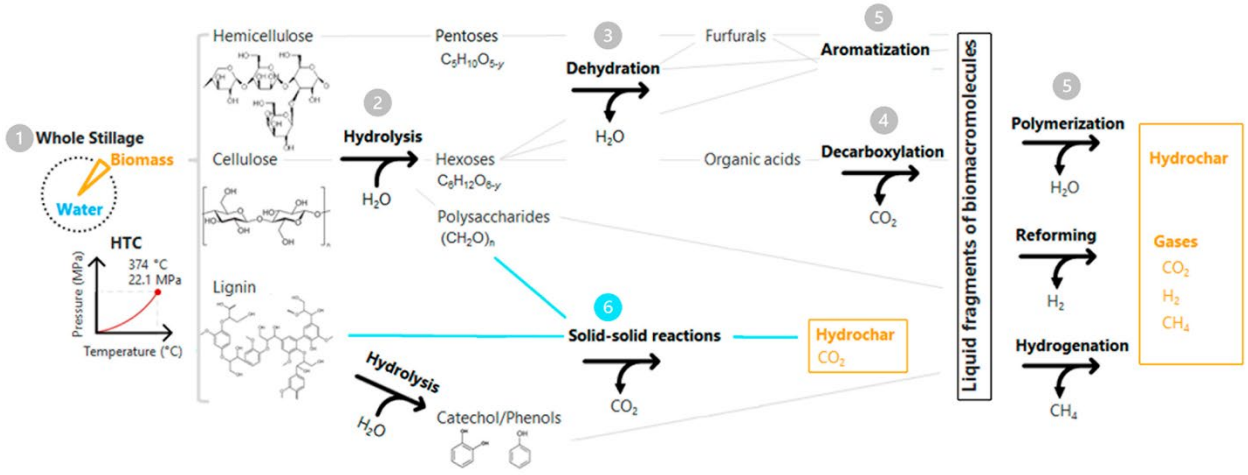

Scheme 1. Chemical pathway for the whiskey stillage HTC.

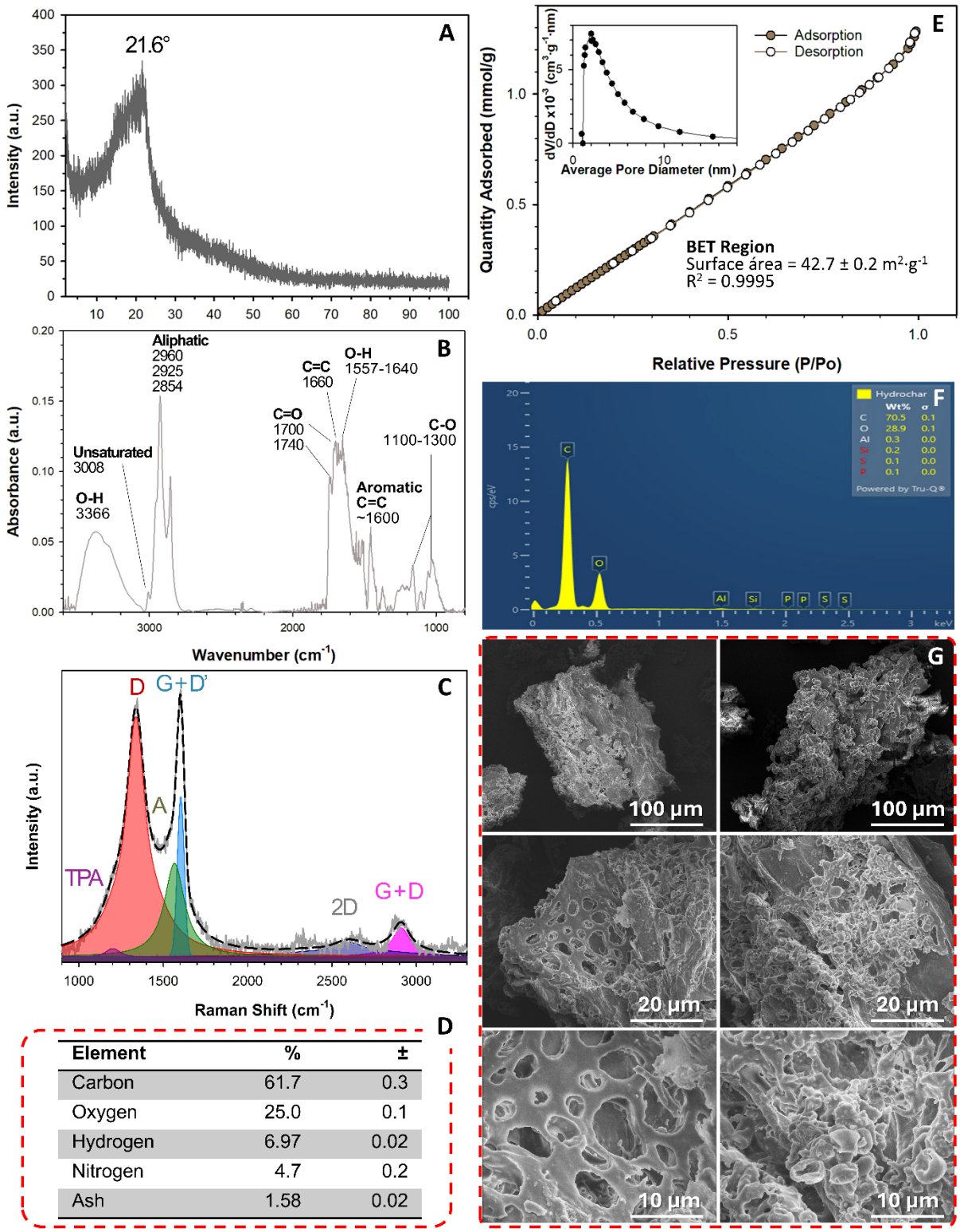

Figure S1. Physicochemical characterization of hydrochar by (A) X-ray diffraction (XRD), (B) Fourier Transformed Infrared spectroscopy (FTIR) in transmission mode using KBr pellets, (C) Raman spectroscopy, (D) total elemental composition*, (E) nitrogen physisorption, (F) Energy-Dispersive X-ray

Spectroscopy (EDS), and (G) Scanning Electron Microscopy (SEM) with scale bars of 100 µm, 20 µm, and 10 µm.

*The total content of carbon, hydrogen, nitrogen, and ashes in the hydrochar (Figure S1D) was determined following ASTM D5373, and the total content of oxygen was calculated by difference.

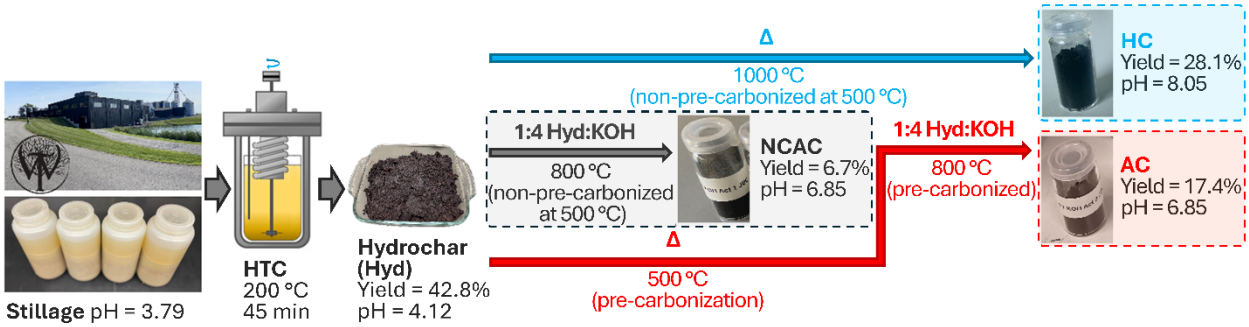

Scheme 2. Synthesis of hard carbon (HC), non-pre-carbonized activated carbon (NCAC), and pre-carbonized activated carbon (AC) from bourbon whiskey stillage.

HC was produced without a pre-carbonization step at 500 °C, as shown in Scheme 2 by the top light blue arrow. The same direct activation approach, indicated by the grey arrow in Scheme 2, decreases the yield of the 1:4 hydrochar to KOH activation by 2.5 times compared to a method that involves a 500 °C pre-carbonization step, marked by the twice-broken red arrow. The pathway to NCAC resulted in inferior synthesis yield and electrochemical performance (Figure S2) compared to AC made via pre-carbonization. The synthesis route for AC reported in this study, which includes the 500 °C pre-carbonization step, is represented in Scheme 2 by the bottom twice-broken red arrow.

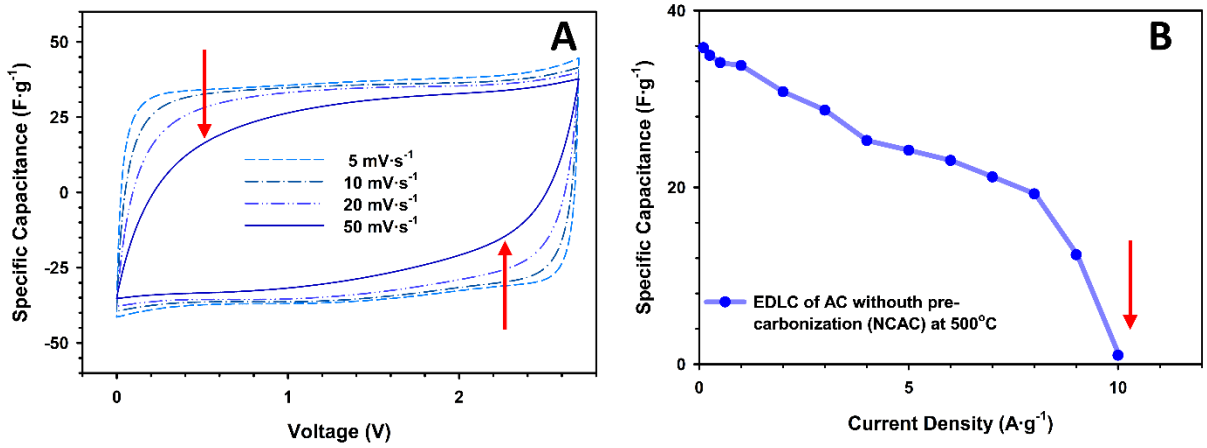

Figure S2. Electrochemical characterization of symmetric EDLC assembled with NCAC or AC without a pre-carbonization step at 500 °C, which presents inferior electrochemical performance than AC as demonstrated by (A) cyclic voltammetry from 5 to 50 $mV \cdot s^{-1}$and (B) galvanostatic charge/discharge at current densities higher than 7 $A \cdot g^{-1}$. Red arrows indicate the specific capacitance fall in devices assembled, as measured by both electrochemical techniques.

Section 2. Raman Spectroscopy

Table S1. HC Raman signal position, assignment, intensity, width, areas, fitting model, and vibration mode explanation.

Raman Shift (cm^{-1})	Assignation*	Intensity (a.u.)	FWHM	Area	Gaussian/ Lorentzian Ratio	Vibration mode
1191.0	TPA (D_4)	9.4	159.1	1956.4	0.51	It is located around 1180-1200 cm^{-1}. Its presence is often associated with hydrogen incorporation, which can lead to the formation of trans-polyacetylene (TPA) chains.[6]
1338.9	D (or D_1)	64.2	146.6	12141.0	0.55	Disordered graphitic lattice (graphene layer edges, A_{1g} symmetry).[7]
1536.5	A (or D_3)	28.0	168.9	5034.6	1.00	Amorphous carbon (pure Gaussian line shape). It originates from various compounds resulting from pyrolytic degradation.[8]
1602.3	G + D' (or D_2)	50.3	56.6	3622.5	0.59	G. Ideal graphitic lattice (E_{2g}-symmetry).[7] D' (if present) overlaps with G-band at the bottom between 1610-1620 cm^{-1}. It is linked to defects within graphitic planes rather than ring-breathing like the D-band (surface graphene layers, E_{2g}-symmetry).[6]
2688.6	2D (or G')	6.2	293.9	2317.2	0.56	2D overtone, arising from a two-phonon lattice vibration process that is activated by double resonance (not defects). It suggests that multilayer graphite (FWHH >> 30 cm^{-1}), high strain and doping (I_{2D}/I_G =0.12), and low crystallinity (I_{2D}/I_D = 0.10). Also indicates the presence of graphene-like layers larger than a few aromatic rings and some degree of π-electron delocalization.[§]
2920.3	G + D	7.1	148.8	1251.0	0.76	It appears because of a combination of D and G phonons between 2900 and 3000 cm^{-1}, whose intensity and position are related to the degree of disorder and crystallinity. I_{D+G}/I_{2D} increases with disorder and finite crystalline size.[§]
3202.1	$2D_2$ (or 2D')	1.1	98.1	124.9	0.89	Weak overtone of the D phonon mode arising from the double-resonance process involving phonons near the K point in the Brillouin zone. The signal is broad (FWHM > 50 cm^{-1}) and low in intensity compared with the 2D (I_{2D2}/I_{2D} = 0.18), which correlates with reduced D/G ratios.[§]

*, § Notes and Raman signal assignations are following Table S2

Table S2. AC Raman signal position, assignment, intensity, width, areas, fitting model, and vibration mode explanation.

Raman Shift (cm^{-1})	Assignation	Intensity (a.u.)	FWHM	Area	Gaussian/ Lorentzian Ratio	Vibration mode
1192.4	TPA (D_4)	2.7	118.3	380.7	0.71	It is located around 1180-1200 cm^{-1}. Its presence is often associated with hydrogen incorporation, which can form transpolyacetylene (TPA) chains.[6]
1341.0	D (or D_1)	27.3	151.7	5922.8	0.28	Disordered graphitic lattice (graphene layer edges, A_{1g} symmetry).[7]
1548.3	A (or D_3)	10.6	166.4	1877.5	1.00	Amorphous carbon (pure Gaussian line shape). It originates from various compounds resulting from pyrolytic degradation.[8]
1603.4	G + D' (or D_2)	20.6	53.0	1383.5	0.6	G. Ideal graphitic lattice (E_{2g}-symmetry).[7] D' (if present) overlaps with G-band at the bottom between 1610-1620 cm^{-1}. It is linked to defects within graphitic planes rather than ring-breathing like the D-band (surface graphene layers, E_{2g}-symmetry).[6]
2711.7	2D	3.3	343.0	1558.3	0.38	Second-order overtone (2D overtone), arising from a two-phonon lattice vibration process that is activated by double resonance (defects do not activate it). Lower in intensity and much broader than HC, it indicates the presence of larger polyaromatic units or microcrystalline inclusions embedded in a largely amorphous matrix.[§]
2949.9	G + D	1.4	91.9	169.9	0.47	Same explanation as in Table S1. The very ill-defined, difficult-to-quantify nature implies tiny crystallites and a high degree of disorder.[§]
3199.4	$2D_2$	0.53	61.2	43.0	0.47	

[§] Observing second-order signals requires high-resolution (< 5 cm^{-1}) and sufficient laser power (9 mW), as used in the present study.[9] Depicting these signals in both HC and AC is less informative than the first-order ones; fitting the entire 2500-3500 cm^{-1} range with Lorentzian/Gaussian profiles after subtracting baseline and sample holder signals helps isolate them and compare between samples.

[§§]Software: Omnic 8.2.0.387. Copyright © 1992-2010 Thermo Fisher Scientific Inc.

[§§§] Assignation and vibration mode explanation from: Ferrari, A.C. and Robertson, J., 2000;[7] Sadezky, A., *et al.*, 2005;[6] and Hodkiewicz, J., 2010.[10]

The spectrum of the sample holder was subtracted from the spectra of HC and AC using the Subtract function. The baseline was corrected using the automatic baseline correction function to remove fluorescence and background noise, and peak intensities and areas were determined. After baseline correction, the ratio of D-band intensity (I_{HC} = 66.4 and I_{AC} = 27.9) to G-band intensity (I_{HC} = 71.3 and I_{AC} = 31.3) serves as a simple, preliminary indicator of structural disorder. However, the Raman spectra were also deconvoluted using the Peak Resolve option, and the resulting areas were used for a more accurate structural analysis. A Gaussian/Lorentzian combination was used as the peak-fitting model, with ratios reported in Tables S1 and S2; 0 corresponds to a pure Lorentzian and 1 to a pure Gaussian.

The integrated areas of deconvoluted peaks (A_D, A_G, A_{TPA}, and A_A) were used to evaluate the degree of graphitization (γ), concentration of defects (δ), crystallite growth (γ/δ), the abundance of TPA-like structures (ϑ), and sp^3-hybridized carbon bonds (α) in the HC as follows:[6, 11, 12]

$$\gamma = \frac{A_G}{A_{Total}} \quad (1)$$

$$\delta = \frac{(A_D + A_A + A_{TPA})}{A_{Total}} \quad (2)$$

$$\vartheta = \frac{A_{TPA}}{A_{Total}} \quad (3)$$

$$\alpha = \frac{(A_A + A_{TPA})}{A_{Total}} \quad (4)$$

In this study, values obtained for γ, δ, γ/δ, ϑ, and α are classified as follows: <0.25 (very low), 0.25–0.50 (low), 0.50–0.75 (high), and >0.75 (very high).

Table S3. Calculated deconvoluted area ratios for HC and AC, and comparison

Material	**γ**	**δ**	**ϑ**	**α**	**γ/δ**	**D band (FWHM/I)**	**G band (FWHM/I)**
HC	0.16	0.84	0.09	0.31	0.19	2.28	1.13
AC	0.14	0.86	0.04	0.24	0.17	5.56	2.57
HC/AC*	1.10	0.98	2.16	1.30	1.12	0.41	0.44

*Red shading highlights ratios higher than 1, while blue shading highlights ratios lower than 1.

Section 3. X-Ray Diffraction

The interplane distances (d_{hkl}) for the samples were calculated based on Bragg's Law:

$$d_{hkl} = \frac{\lambda}{2\sin\theta_{hkl}} \quad (5)$$

Where λ is the radiation wavelength (Cu K_α = 0.154059 nm) and θ is the reflection angle for the plane with Miller indices (hkl).

The Scherrer equation determines the average crystalline thickness and average diameter:

$$(L_c \text{ or } L_a) = \frac{\kappa\lambda}{(B\cos\theta)} \quad (6)$$

Where L_c is the dimension of crystallites in the perpendicular plane (thickness along the *c*-axis) and L_a the crystallite dimension in the *ab*-plane (average crystallite diameter). B is the full width at half maximum (FWHM), in radians of theta, and κ is a constant. L_c is determined using the data from the (002) region and κ = 0.89, while L_a is determined based on data from the (100) region and κ = 1.84.[13, 14] The same software used for Raman data analysis is used to fit the XRD experimental data to Gaussian and Lorentzian curves. (Omnic 8.2.0.387. Copyright © 1992-2010 Thermo Fisher Scientific Inc).

HC XRD analysis

(002) Hump-Gaussian	(100) Hump-Lorentzian
2θ = 23.7°	2θ = 43.8°
d_{002} = 0.375 nm	d_{002} = 0.207 nm
FWHM = 7.43° (7.43π/180 ≈ 0.1296 rad)	FWHM = 5.47° (5.47π/180 ≈ 0.1296 rad)
Apparent L_c = 1.08 nm (1.08/0.375 ≈3 stacked graphene layers)	Apparent L_a = 3.2 nm lateral domains

The Gaussian description of (002) region is due to the distributed interlayer spacing, where its position indicates the average *d*-spacing. The (100) region is broader and less well-defined by a single Lorentzian, which can be attributed to an overlap of (100)/(101) features in turbostratic carbons.[15] Given the broadness and weakness of both diffraction signals, the resulting LC and La

are in the low-nanometer range, indicating only a few stacked layers (~3) and nanometric lateral graphitic domains (~3 nm) embedded in a largely disordered matrix.

Section 4. Hard Carbon Characterization

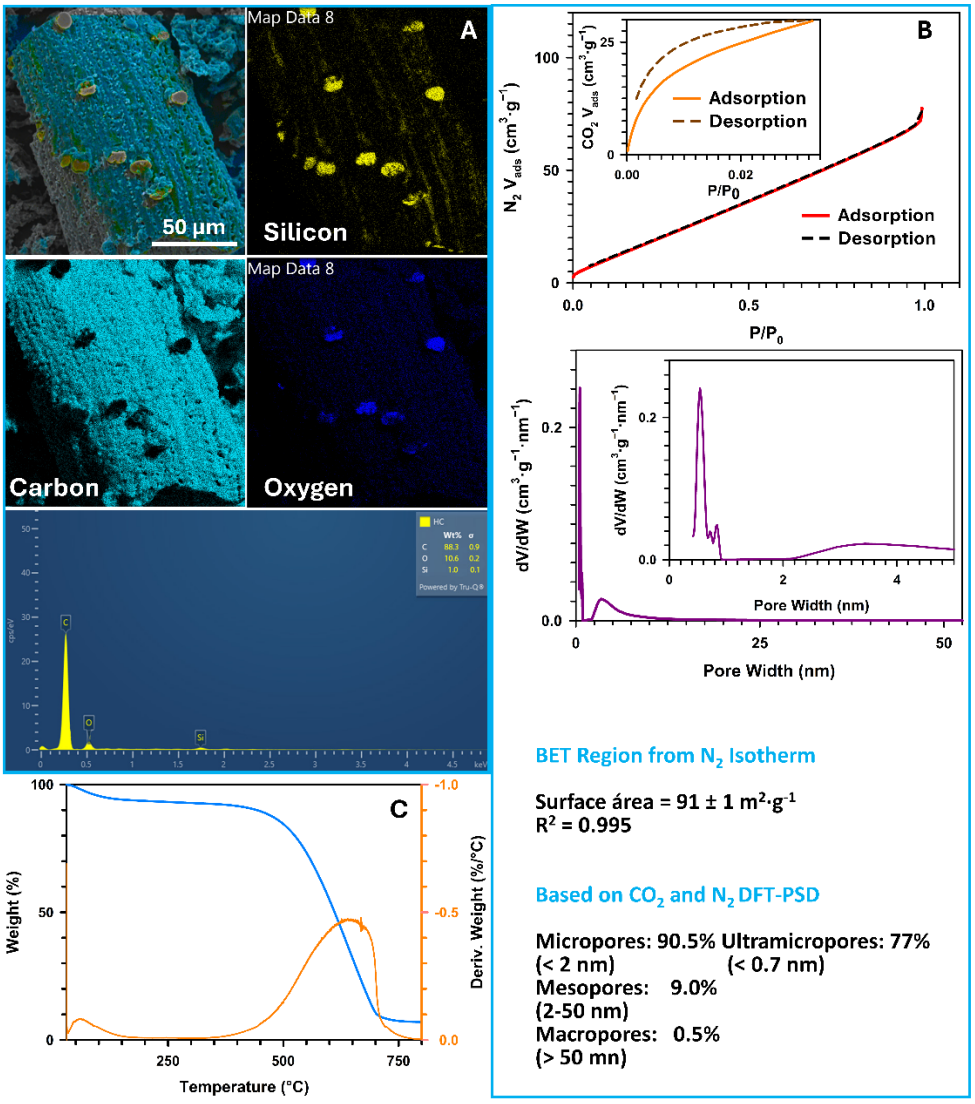

Figure S3. Physicochemical characterization of HC by (A) SEM-EDS, (B) nitrogen and carbon dioxide adsorption and pore size distribution[§], and (C) thermogravimetric analysis (TGA)[*] under air.

[§]For the pore size distribution of hard carbon, combined CO_2 (273 K) and N_2 (77 K) experimental data were fitted to the models **DFT/Slit/CO2@273-Carbon Slit Pores by NLDFT**, and **DFT/Slit/N2@77 on Carbon Slit Pores by NLDFT** implemented in Flex version 6.03 (dae888677) software from Micromeritics Instrument Corporation. The relative pore-volume contribution of each pore-size range is calculated by integration of the dV/dW curve across the selected pore-width interval and normalizing by the total integrated pore volume.

[*]The thermogravimetric curve (Figure S3C) was recorded using a high-resolution TA Instrument Q5500, operated at a heating rate of 10 °C·min^{-1}. The samples were heated from room temperature to 800 °C under an air flow of 10 mL·min^{-1}.

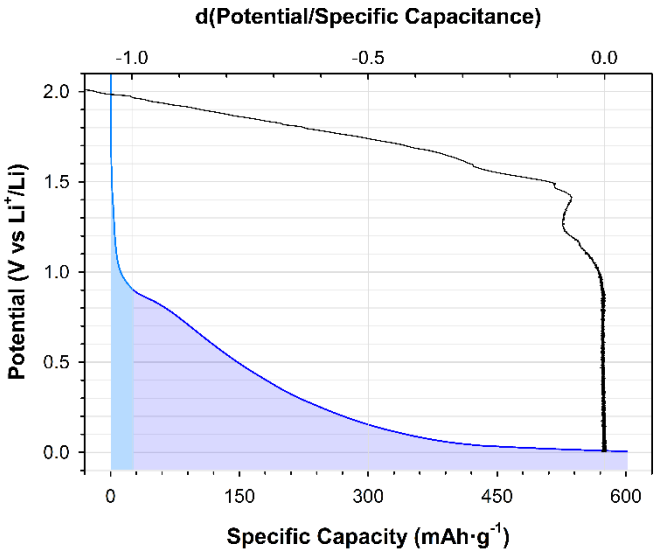

Figure S4. Detailed analysis of the Li-ion storage mechanisms and solid electrolyte interphase (SEI) formation during the first cycle at 0.05 C.

Key features of the different ways lithium ions interact with the complex structure of the HC are present in the charge curve of Figure S4, which shows **three characteristic stages**. The **first stage**, characterized by a high potential slope from 2.0 to 0.88 V vs. Li^+/Li, accounts for 16% of the capacity. This first stage is attributed to SEI formation, surface adsorption, and intercalation.[16] The SEI formation should be the dominant process during the very first discharge cycle at high potentials. When the HC potential drops, the electrolyte components become thermodynamically unstable and are reduced on the surface. Chemical calculations reveal that VC's LUMO energy is lower than EC and DMC due to its double bond, leading it to reduce first on the HC surface and form a stable, thin, ionically conductive SEI passivation layer.[17] This is an irreversible process that consumes some lithium ions and electrolyte over the large 91±1 $m^2 \cdot g^{-1}$ surface area of the HC, resulting in significant initial capacity loss (38.6 %). However, a well-formed SEI indicates good HC-electrolyte compatibility and is crucial, as it prevents continuous electrolyte decomposition and enables stable cycling.

The **second stage** consisted of an extended sloping region (82% of capacity) from 0.88 to 0.05 V, where lithium ions mainly adsorb to the surface of the disordered layers and insert between them (intercalation). This is analogous to intercalation in graphite; however, the disordered nature of HC creates a broad distribution of energy levels, resulting in a sloped profile rather than the distinct plateau seen in graphite. Finally, the **third stage** is a small (2%) low-potential plateau region, from 0.05 to 0.005 V, which has been linked to the filling of nanopores and voids within the HC structure, without lithium plating.

Section 5. Activated Carbon Characterization

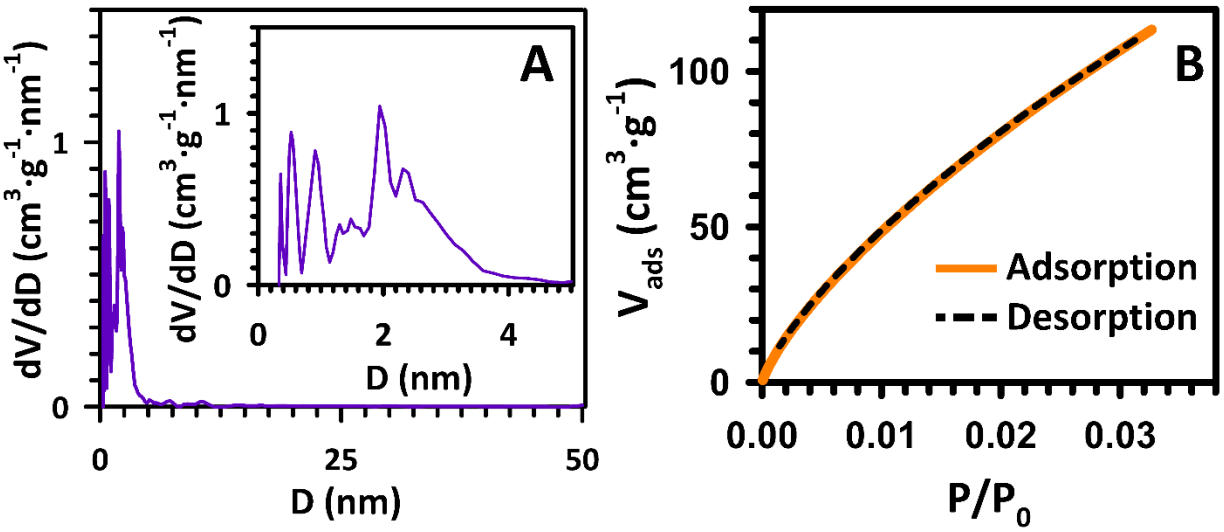

Figure S5. Pore size distribution (PSD) calculated from activated carbon (AC) nitrogen and carbon dioxide adsorption experiments using the two dimensional-finite pore (2D) Non-Local Density Functional Theory model (2D-NLDFT, Carbon, N_2, 77), represented by the first derivate of the volume (dV) and the first derivative of the average pore diameter (dD) vs the average pore diameter (D), showing the large abundance of ultramicropores (<0.7 nm), micropores (<2 nm) and as well as small mesopores (2-5 nm) compared to larger mesopores (5-30 nm). CO_2 adsorption isotherm at 273 K (B), which describes the amount of CO_2 adsorbed (V_{ads}) as a function of relative pressure (P/P_0) and provides a highly sensitive evaluation of the AC ultra-microporosity.

For the pore size distribution of activated carbon, combined CO_2 (273 K) and N_2 (77 K) experimental data were fitted to the models **DFT/Slit/CO2@273-Carbon Slit Pores by NLDFT**, and **DFT/Slit/N2@77 on Carbon Slit Pores by NLDFT** implemented in Flex version 6.03 (dae888677) software from Micromeritics Instrument Corporation.

Section 6. Symmetric EDLCs Performance

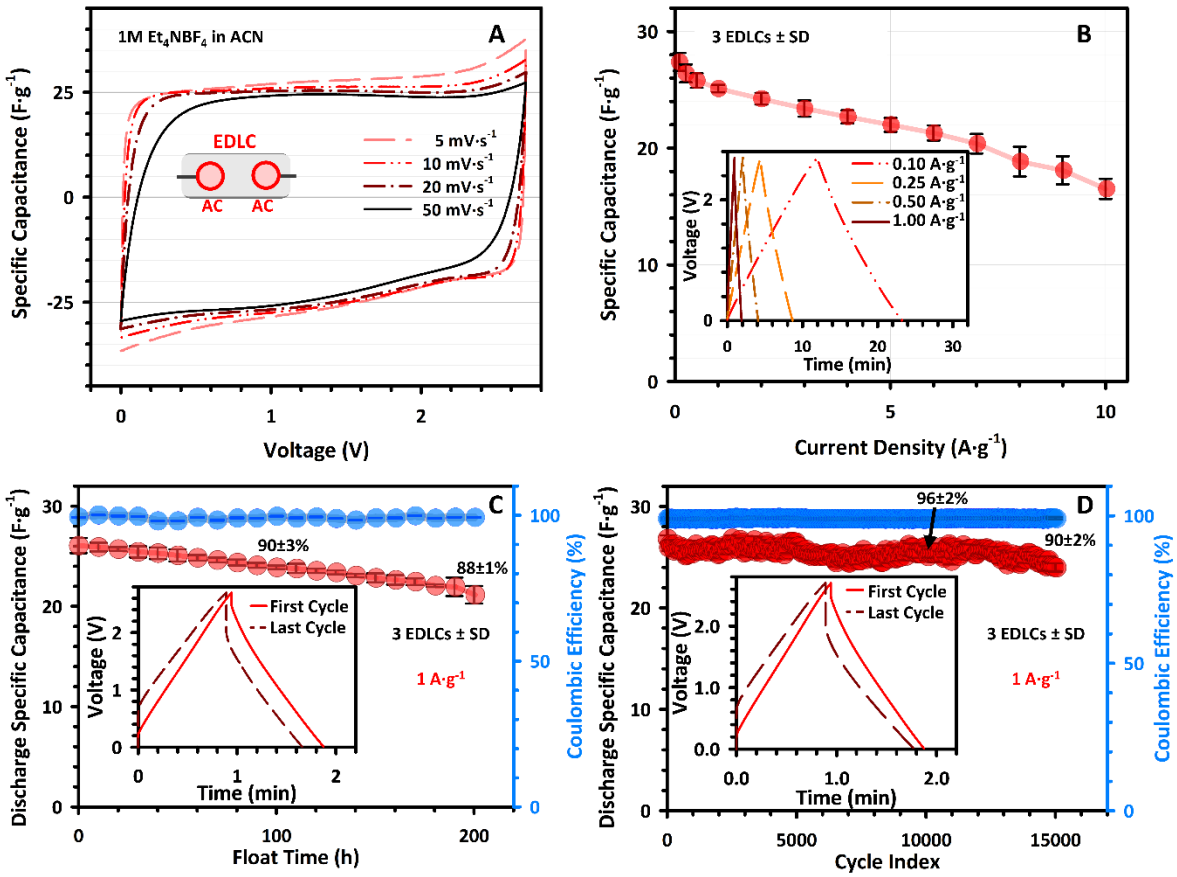

Figure S6. Electrochemical performance of AC-based electrodes in symmetrical Electric Double Layer Capacitors (EDLCs) using 1 M Et_4NBF_4 in ACN. (A) Cyclic voltammograms recorded at scan rates from 5 to 50 $mV \cdot s^{-1}$. Inset: schematic of the EDLC configuration (AC||AC). (B) Galvanostatic charge-discharge curves at current densities from 0.1 to 10 $A \cdot g^{-1}$; inset shows representative profiles at 0.1, 0.25, 0.50, and 1.0 $A \cdot g^{-1}$. (C) Float test at 2.7 V over 200 h, with capacitance retention (%) after 100 and 200 h. Inset: representative galvanostatic curves at 1.0 $A \cdot g^{-1}$ before and after the test. (D) Cycling stability at 1 $A \cdot g^{-1}$, showing capacitance retention after 10,000 and 15,000 cycles. Inset: representative galvanostatic curves before (first cycle) and after (last cycle) the test. Error bars for specific capacitance in B, C, and D represent the standard deviation across three independent EDLC devices.

Section 7. Lithium-ion Capacitors Optimization

To compensate for the initial irreversible capacity loss, a prelithiation strategy is used to supply extra lithium to the HC anode (sections 2.3 and 3.4) before LiC formation assembly.

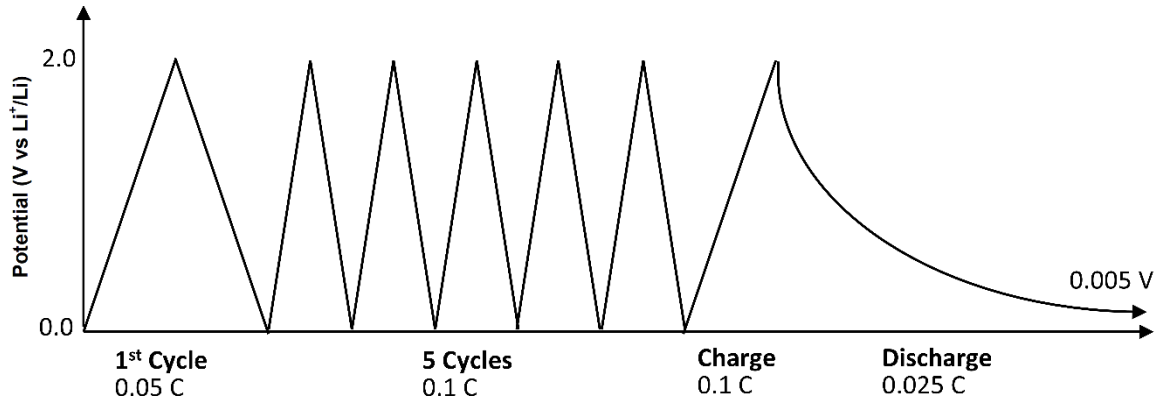

Scheme 3. HC Prelithiation strategy

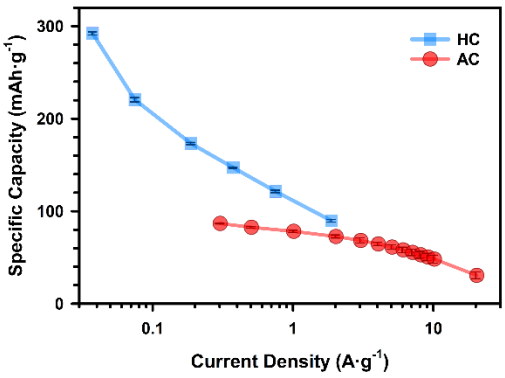

HC-based Electrode			AC-based Electrode		
Current Density (A·g⁻¹)	Average Specific Capacity (mAh·g⁻¹)	SD (mAh·g⁻¹)	Current Density (A·g⁻¹)	Average Specific Capacity (mAh·g⁻¹)	SD (mAh·g⁻¹)
0.0372	292	2	0.3	86.7	0.6
0.0744	221	2	0.5	83	1
0.186	173	1	1	78	1
0.372	147.2	0.6	2	73	2
0.744	121	1	3	68	3
1.86	90	1	4	65	2
			5	61	2
			6	58	3
			7	55	3
			8	53	4
			9	50	4
			10	48	4
			20	31	4

Figure S7. Average specific capacity of HC and AC electrodes evaluated in half-cells versus Li/Li^+ in LP30-2VC* at variable current densities, used to define the active mass ratio in the LiC devices. Data is presented on a semi-logarithmic plot (current density axis) to represent the wide current density range, with error bars indicating the standard deviation across three electrodes.

*LP30-2VC: 1 M hexafluorophosphate in a 1 v/v ethylene carbonate and dimethyl carbonate containing 2 wt% of vinylene carbonate (VC).

Figure S7 shows that specific capacities of HC and AC are significantly different at low current densities, with 292 $mAh \cdot g^{-1}$ at 0.04 $A \cdot g^{-1}$ for HC-based electrodes that are 3.37 times higher than the 86.7 $mAh \cdot g^{-1}$ at 0.3 $A \cdot g^{-1}$ for AC. However, at high current densities, the specific capacities of HC and AC approach each other, with a ratio of 1.2:1 at 2 $A \cdot g^{-1}$ and expected to reach approximately 1.14 at 3 $A \cdot g^{-1}$. A 1:1 mass ratio should enable near-stoichiometric matching at high rates, with HC slightly oversized to prevent lithium plating.

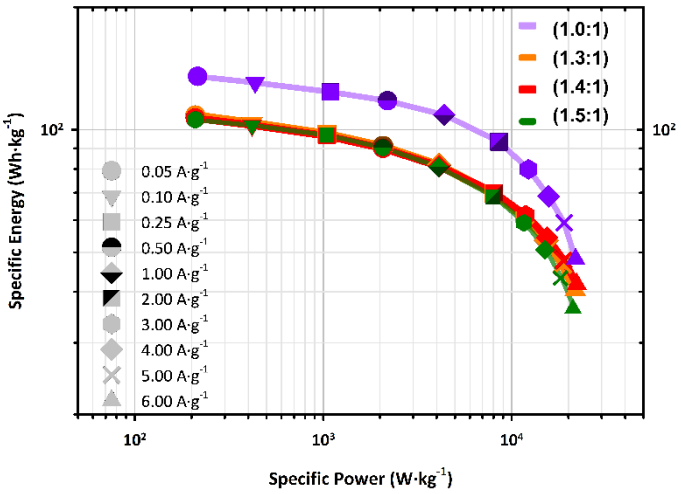

Figure S8. Ragone plot showing the relationship between gravimetric energy and power densities for LiC devices operated at current densities from 0.05 to 6 $A \cdot g^{-1}$, with HC: AC mass ratios from 1.0 to 1.5. An HC: AC mass ratio of 1 demonstrates superior performance across all current densities tested. Specific energy and power densities are normalized to the combined total electrode mass.

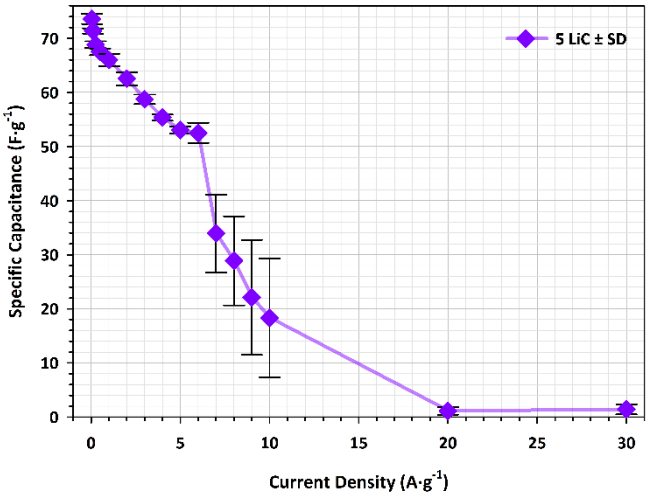

Figure S9. Electrochemical performance of LiC devices at current densities from 0.05 to 30 $A \cdot g^{-1}$, where values of specific capacitance show poor reproducibility at current densities beyond 6 $A \cdot g^{-1}$ illustrated by values of relative standard deviation (RSD) in % higher than 21%.

Therefore, the electrochemical performance of LiC devices is reported only from 0.05 to 6 $A \cdot g^{-1}$ in the main manuscript, as this is the range in which devices demonstrated reproducible behaviour.

Table S4. Specific Capacitances ± standard deviation (SD) of five devices (*n* = 5) and RSD in % at current densities from 0.05 to 30 $A \cdot g^{-1}$.

Current Density ($A \cdot g^{-1}$)	Specific Capacitance ($F \cdot g^{-1}$)	SD ($F \cdot g^{-1}$)	RSD (%)
0.05	73.6	0.9	1
0.1	71.4	0.5	1
0.25	68.83	0.02	1
0.5	67.5	0.6	1
1	66	1	1
2	63	1	2
3	58.7	0.9	1
4	55.3	0.6	1
5	53.1	0.7	1
6	53	2	4
7	34	7	21
8	29	8	29
9	22	11	48
10	18	11	60
20	1.1	0.7	61
30	1.4	0.9	66

Table S5. Comparison of representative distillery/fermentation-waste-based EDLCs

Precursor	Activation Method Surface Area ($m^2 \cdot g^{-1}$)	Electrolyte	Voltage (V)	Capacitance ($F \cdot g^{-1}$)	Energy density ($Wh \cdot kg^{-1}$) / Power density ($W \cdot kg^{-1}$)	Stability	Note	Reference
Bourbon stillage	HTC 4:1 KOH, 800 °C 2,862	1 M Et_4NBF_4/ACN	2.7	25.1 ± 0.3 at 1 $A \cdot g^{-1}$ 17 ± 2 at 10 $A \cdot g^{-1}$	23.8 at 270 1.9 at 9,200	**96% after 10,000 cycles**	No dopant, template, or pretreated precursor	**This work**
Wine waste	4:1 KOH, 800 °C 2,467	1 M Et_4NBF_4/ACN and EMINTFSI	2.7-3.1	65 (pristine) 130 (composite)	27 at 13,026	70% after 6,000 cycles	Graphene composite	Urena-Torres, V., et al. ChemEngineering 6 (2022).[18]
Brewery waste	1:2 and 1:4 KOH, 800 °C 3,600	1M $TEMABF_4$ in ACN	2.7	45 at 0.5 $A \cdot g^{-1}$ 41 at 10 $A \cdot g^{-1}$	45 at 675	85% after 200 h of float test at 2.7V		Magar, Sandesh Darlami, et al. *Electrochimica Acta* 446 (2023): 142104.[19]
Corn-based ethanol distillery grains	950 and 1050 °C 0.075 $mol \cdot g^{-1}$ KOH 2,959 2,684	1M $TEMABF_4$ in ACN	3	150 70 at 0.5 $A \cdot g^{-1}$	No provided	88% after 1,000 cycles 64% after 1000 cycles		Jin, Hong, et al. *Journal of Environmental Chemical Engineering* 2.3 (2014): 1404-1409.[20]
Japanese distilled liquor (Shochu) waste	700 °C 8 $mol \cdot L^{-1}$ KOH 2,434	1M $TEA \cdot BF_4$/PC	2.5	152 at 0.1 $mA \cdot cm^{-2}$	30 at 200	96% after 2,000 cycles		Eguchi, Takuya, et al. *Journal of Cleaner Production* 259 (2020): 120822.[21]
Sugarcane **bagasse**	850 °C, 100 cm3·min−1 CO2	1M $TEMABF_4$ in ACN	2.7	42	10 at 2,500	80% after 10,000 cycles		Somyanonthanakun, Wuttichai, et al. *Sustainability* 15.6 (2023): 5566.[22]

Table S6. Electrochemical performance of dual-carbon LiCs based on biomass

Anode	Cathode	Precursor	Single source	AC Surface Area ($m^2 \cdot g^{-1}$) /Electrolyte	$Energy_{max}$ ($Wh \cdot kg^{-1}$)/ $Power_{max}$ ($kW \cdot kg^{-1}$)	Stability	Note	Reference
HC — pyrolysis 1000°C, N_2	AC — KOH 4:1, 800°C, N_2	Bourbon distillery stillage (single liquid waste; pH 3.79; 89.95% H_2O)	Yes	2,862 LP30-2VC	**135 / 0.2** **48 / 22**	**83% after 5,000 cycles 69% after 10,000 cycles at 3 $A \cdot g^{-1}$**	Energy and power referred to the total mass of the electrodes	**This work**
HC — pyrolysis 112 mAh/g at 10C	KOH-AC from HC 2399 m^2/g	Pinus Radiata (forestry waste)	Yes	2,399 1 M $LiPF_6$ in a 1:1 vol mix of EC: DMC	111 / 0.51 52 / 24.4	70% after 5,000 and 60% after 10,000 cycles at 10C	(Stability calculated relative to the anode)	Rodriguez-Romero, Jon, Idoia Ruiz de Larramendi, and Eider Goikolea. *Journal of Power Sources* 629 (2025): 235961.[23]
HC — pyrolysis 1000°C, N_2	1:2 and 1:4 KOH-AC, 800 °C 3,600	Brewery waste spent grains	Yes	3,600 LP30	152 /0.312 34 / 12	72% after 8,000 cycles at 1 $A \cdot g^{-1}$	Energy and power referred to the active electrode mass	Magar, Sandesh Darlami, et al. *Electrochimica Acta* 446 (2023): 142104.[19]
HC — pyrolysis 1000°C, Ar	AC — 1:2 KOH, 900 °C	Petroleum coke	Yes	1,952 1 M $LiPF_6$ 1:1:1 wt % mix of EC:DMC:DEC	80 / 8.4	85% capacity retention after 10,000 cycles at 1 $A \cdot g^{-1}$		Veluri, Pavan S., et al. *Energy & Fuels* 35.10 (2021): 9010-9016.[24]
Commercial graphite	AC — KOH, 900 °C, 1 h	*Roselle* plant stem	No	1,826 1 M $LiPF_6$ electrolyte EC:DEC solvent	125 / 0.069	69% capacity retention after 2,500 cycles		Nanaji, Katchala, et al. *Global Challenges* 6.10 (2022): 2200082.[25]

References

1. D. Lachos-Perez, P. C. Torres-Mayanga, E. R. Abaide, G. L. Zabot and F. De Castilhos, *Bioresour. Technol.*, 2022, **343**, 126084.
2. M. Heidari, A. Dutta, B. Acharya and S. Mahmud, *J. Energy Inst.*, 2019, **92**, 1779–1799.
3. X. Zhuang, J. Liu, Q. Zhang, C. Wang, H. Zhan and L. Ma, *Renew. Sustain. Energy Rev.*, 2022, **154**, 111877.
4. J. González-Arias, M. E. Sánchez, J. Cara-Jiménez, F. M. Baena-Moreno and Z. Zhang, *Environ. Chem. Lett.*, 2021, 1–11.
5. S. Sivaprasad, A. Manandhar and A. Shah, *Journal*, 2021.
6. A. Sadezky, H. Muckenhuber, H. Grothe, R. Niessner and U. Pöschl, *Carbon*, 2005, **43**, 1731–1742.
7. A. C. Ferrari and J. Robertson, *Phys. Rev. B*, 2000, **61**, 14095.
8. D. Goers, M. Baertsch, A. Wuersig, L. Hardwick and P. Novak, *In situ Raman Studies of Phenolic Resin based Hard Carbon*, Springer, 2003.
9. Z. Li, L. Deng, I. A. Kinloch and R. J. Young, *Prog. Mater. Sci.*, 2023, **135**, 101089.
10. J. Hodkiewicz, *Thermo Fisher Sci.*, 2010, 51946.
11. H. D. Asfaw, R. Gond, A. Kotronia, C.-W. Tai and R. Younesi, *Sustainable Mater. Technol.*, 2022, **32**, e00407.
12. A. Cuesta, P. Dhamelincourt, J. Laureyns, A. Martínez-Alonso and J. D. Tascón, *Carbon*, 1994, **32**, 1523–1532.
13. B. Warren, *Phys. Rev.*, 1941, **59**, 693.
14. D. J. Lim, N. A. Marks and M. R. Rowles, *Carbon*, 2020, **162**, 475–480.
15. Z. Li, C. Lu, Z. Xia, Y. Zhou and Z. Luo, *Carbon*, 2007, **45**, 1686–1695.
16. S. K. Saju, S. Chattopadhyay, J. Xu, S. Alhashim, A. Pramanik and P. M. Ajayan, *Cell Rep. Phys. Sci.*, 2024, **5**.
17. R. Lundstrom, N. Gogoi, T. Melin and E. J. Berg, *J. Phys. Chem. C*, 2024, **128**, 8147–8153.
18. Ureña-Torres V, Moreno-Fernández G, Gómez-Urbano JL, Granados-Moreno M, Carriazo D. ChemEng. 2022;6(4):49.
19. Magar SD, Leibing C, Gómez-Urbano JL, Cid R, Carriazo D, Balducci A. Electrochimica Acta. 2023;446:142104.
20.. Jin H, Wang X, Gu Z, Anderson G, Muthukumarappan K. Chem Eng. 2014;2(3):1404-9.
21. Eguchi T, Tashima D, Fukuma M, Kumagai S. J. Clean. Prod. 2020;259:120822.
22. Somyanonthanakun W, Greszta A, Roberts AJ, Thongmee S. Sustainability. 2023;15(6):5566.
23. Rodríguez-Romero J, de Larramendi IR, Goikolea E. J. Power Sources. 2025;629:235961.
24. Veluri PS, Katchala N, Anandan S, Pramanik M, NarayanSrinivasan K, Ravi B, N. Rao T. Energy & Fuels. 2021;35(10):9010-6.
25. Nanaji K, Pappu S, Anandan S, Rao TN. Global Challenges. 2022 (10):2200082.